Optical Materials: X 19 (2023) 100242

Contents lists available at ScienceDirect

Optical Materials: X

journal homepage: www.elsevier.com/locate/omx

Z-Scan theory for thin film measurements: Validation of a model beyond the standard approach using ITO and HfO_2

Andrea Tognazzi [a,b], Paolo Franceschini [b,c], Thi Ngoc Lam Tran [d,e], Alessandro Chiasera [d], Maria Antonietta Vincenti [b,c], Alfonso Carmelo Cino [a], Neset Akozbek [f], Michael Scalora [g], Costantino De Angelis [b,c,*]

[a] Department Engineering, University of Palermo, Viale delle Scienze ed. 10, Palermo, 90128, Italy
[b] Consiglio Nazionale delle Ricerche - Istituto Nazionale di Ottica, Sede di Brescia, Via Branze 45, Brescia, 25123, Italy
[c] Department of Information Engineering, University of Brescia, Via Branze 38, Brescia, 25123, Italy
[d] IFN-CNR CSMFO Lab. and FBK Photonics Unit, Via alla Cascata 56/C, Trento, 38123, Italy
[e] Department of Physics, Politecnico di Milano, Piazza Leonardo da Vinci 32, Milano, 20133, Italy
[f] U.S. Army Space and Missile Defense Command, Technical Center, P.O. Box 1500, Huntsville, AL 35807-3801, USA
[g] DEVCOM Aviation and Missile Center, Bldg. 7804 Redstone Arsenal, AL 35898-5000, USA

ARTICLE INFO

Keywords:
Z-scan
ITO
Hafnia
Nonlinear optics

ABSTRACT

The Z-Scan technique is an easy and widespread approach to evaluate the nonlinear optical coefficient of materials. However, the evaluation of the same coefficients for thin films requires complex experimental setups that allow to remove the contributions of the substrate. Here, we propose a simple, yet effective, theoretical approach that allows to include the substrate contribution to the focusing effect when scanning along the propagation axis. The proposed method therefore removes the need of complex experimental setups and paves the way for a simpler retrieval of optical properties of complex nanostructures.

1. Introduction

Delving into nonlinear optical properties of materials has been one of the top priorities since the first demonstration of second harmonic generation [1]. Nonlinear optics significantly impacts many applications, ranging from optical parametric amplifiers and fiber optics to communications and lasers, to name a few [2,3]. For this reason, the evaluation of the nonlinear optical properties of materials and understanding light-matter interactions at the nanoscale are of paramount importance when attempting to design devices that must function at the macroscopic level. The knowledge of such parameters becomes particularly relevant in ultrashort pulsed laser applications, where high local fields and intensities are involved, triggered by self-focusing, geometrical resonances, or epsilon-near-zero conditions.

The Kerr effect is a well-known phenomenon which is routinely exploited in mode-locked lasers and soliton generation [4]. The most common method used to quantify the third order nonlinear refractive index is the Z-Scan technique. Although it has significant limitations in that it cannot adequately describe high scattering and absorption environment, and is restricted to operate within the bandwidth of the pump, it is nevertheless efficient and simple to implement experimentally [5–7]. When performing a Z-scan measurement, the sample is moved along the propagation direction of a focused gaussian beam while the transmitted intensity is recorded, with and without an iris in front of the detector. However, while evaluating and quantifying the nonlinear properties of a medium is relatively simple for bulk materials, the same cannot be said for thin films because they are substantially different from their bulk counterparts in both their intrinsic properties and nonlinear sources, and their geometrical configuration. In this sense, a dual-arm geometry [8], a two beam experiment [9], and a reflection setup [10] were previously proposed to remove the possible contribution of a substrate having thickness equal or greater than the thin film under investigation. Under those circumstances, the setup becomes more complex, difficult to operate and requires specific post-processing of the measured signals. For the single-arm geometry, a model including internal reflections based on mean field theory was proposed [11]. However, for thin films that do not display geometrical (or Fabry–Perot) resonances and linear refractive indexes nearly matched to that of the substrate, it is possible to employ a simple model that neglects internal reflections which also prevent us from imposing consistency conditions as in [11].

Here, we show that the traditional Z-Scan analysis may fail by two orders of magnitude even when evaluating thin-films nonlinearities

* Corresponding author at: Consiglio Nazionale delle Ricerche - Istituto Nazionale di Ottica, Sede di Brescia, Via Branze 45, Brescia, 25123, Italy.
E-mail addresses: andrea.tognazzi@unipa.it (A. Tognazzi), paolo.franceschini@ino.cnr.it (P. Franceschini), costantino.deangelis@unibs.it (C. De Angelis).

https://doi.org/10.1016/j.omx.2023.100242
Received 23 February 2023; Received in revised form 6 June 2023; Accepted 12 June 2023
Available online 16 June 2023

and not only when plasmonic metasurfaces are involved [12]. We thus introduce a post-processing method to overcome this shortcoming without resorting to more complicated experimental setups or mean-field approaches, or determination of conversion efficiencies. Specifically, we first extend the Z-Scan model to include the nonlinear contribution of the substrate to appropriately quantify the nonlinear properties of the film, and then perform experimental measurements. To test our model, we measure the nonlinear response of ITO and compare it with values reported in the literature [7,13]. We also characterize a hafnia (HfO_2) thin film at 1035 nm because it has a wide transparency region, and it has significant potential applications for nonlinear optical on-chip integration, enjoys established fabrication techniques and it is compatible with existing technologies [14–16].

2. Model

In Fig. 1a we report a sketch of typical setup adopted in Z-Scan experiments, as first presented in [5]. A polarized gaussian beam propagates in the direction of the z-axis and the amplitude of the incident electric field (not perturbed by the sample) is given by

$$E(z,r,t) = E_0(t)\,\frac{w_0}{w(z)}\,\exp\left[-\frac{r^2}{w^2(z)} - \frac{ikr^2}{2R(z)}\right] e^{-i\phi(z,t)} \tag{1}$$

where r is the distance from the beam axis, w_0 is the beam waist radius, $w(z)$ is the beam radius in z, $R(z)$ is the radius of curvature of the wavefront at z, $k = 2\pi/\lambda$ is the wave number, λ is the wavelength, and $\phi(z,t)$ is the phase. The expressions of the beam radius and curvature are

$$\begin{aligned} w(z) &= w_0 \cdot \sqrt{1+\left(\frac{z-z_f}{z_R}\right)^2} \quad \text{and} \\ R(z) &= (z-z_f)\cdot\left[1+\left(\frac{z_R}{z-z_f}\right)^2\right], \end{aligned} \tag{2}$$

respectively, where z_f is the focus position and $z_R = kw_0^2/2$ is the Rayleigh range (diffraction length of the beam).

From the experimental point-of-view of the Z-Scan technique [5], the transmittance of a focused beam through a nonlinear medium as a function of the sample position z (with respect to the focal plane) provides information on the nonlinear refractive index n_2 provided that $L < z_R$, with L being the sample thickness, and n_2 is related to the refractive index n by

$$n = \tilde{n}_0 + \frac{n_2}{2}\,|E|^2, \tag{3}$$

where $\tilde{n}_0 = n_0 + i\kappa$ is the linear complex refractive index. In particular, the measured transmittance through an aperture of finite size in far field (closed aperture, CA, trace) mainly depends on the focusing/defocusing properties of the material (ascribed to the real part of n_2), while in absence of any aperture (open aperture, OA, trace) the nonlinear absorption (imaginary part of n_2) mainly dominates. The theoretical model developed in [5] provides a powerful tool capable to retrieve the nonlinear coefficients in the case of a sample consisting in a uniform bulk material. However, the experimental results obtained in the case of samples consisting in a thin film deposited on a substrate, both endowed by a nonlinear refractive index, might not be fully reproduced.

Therefore, in analogy with [5], we apply a gaussian beam decomposition to include in our model the presence of a thin film. In our model, the sample consists in a thin film (F) deposited on a substrate (S), as depicted in Fig. 1b. We introduce the coordinate $\tilde{z}$ which represents the propagation depth inside the sample. The film (substrate) occupies the region $0 < \tilde{z} < d$ ($d < \tilde{z} < d + L$). When the electric field propagates in the sample, the intensity $I = nc\varepsilon_0|E|^2/2$ and the phase variation $\Delta\phi$ are governed by the following initial values problems:

$$\begin{cases} \dfrac{\mathrm{d}\Delta\phi}{\mathrm{d}\tilde{z}} = k\,\gamma^{(h)}\,I \\ \dfrac{\mathrm{d}I}{\mathrm{d}\tilde{z}} = -\alpha_0^{(h)}\,I - \beta^{(h)}\,I^2 \end{cases} \qquad h = F,\ S \tag{4}$$

where $\alpha_0^{(h)}$ is the linear part of the absorption coefficient, $\gamma^{(h)}$ and $\beta^{(h)}$ are the real and imaginary part of the complex nonlinear refractive index of the hth medium, respectively. The differential problem in Eq. (4) is solved taking into account suitable initial conditions for $\Delta\phi$ and I (see Appendix A).

The electric field pattern at the aperture in z_{FF} is:

$$\begin{aligned} &\mathcal{E}_{\mathrm{AP}}(z,r,t,z_D) = \\ &\quad t_{SA}\,t_{FS}\,t_{AF}\,E(z,r=0,t)\,e^{-\alpha_0^{(F)}\,d/2}e^{-\alpha_0^{(S)}\,L/2}\sum_{m,l=0}^{\infty} M_m\,P_m\,L_l\,J_l\,\frac{w_{q0}}{w_q} \\ &\quad \times \exp\left(-\frac{r^2}{w_q^2} - \frac{ikr^2}{2R_q} + i\theta_q\right), \end{aligned} \tag{5}$$

where $q = m + l$, z_D is the propagation distance in free space from the sample to the aperture plane,

$$\begin{aligned} &g = 1 + \frac{z_D}{R(z)}, \quad w_{q0}^2 = \frac{w^2(z)}{2q+1}, \quad d_q = \frac{kw_{q0}^2}{2}, \quad w_q^2 = w_{q0}^2\left[g^2 + \frac{z_D^2}{d_q^2}\right], \\ &\theta_q = \arctan\left[\frac{z_D/d_q}{g}\right], \qquad R_q = z_D\left[1 + \frac{g\,d_q^2}{z_D^2 + g\,(g-1)\,d_q^2}\right], \\ &M_m = \frac{1}{m!}\left[i\,\beta^{(F)}\,|t_{AF}|^2\,\psi(z,t)\,\mathcal{L}^{(F)}(d)\right]^m, \\ &P_m = \prod_{v=1}^{m}\left[\left(\frac{k\gamma^{(F)}}{\beta^{(F)}} - \frac{k\gamma^{(S)}}{\beta^{(S)}}\right) + i\,(v-1)\right], \\ &L_l = \frac{1}{l!}\left\{i\,|t_{AF}|^2\,\psi(z,t)\left[\beta^{(F)}\,\mathcal{L}^{(F)}(d) + \beta^{(S)}\,\mathcal{L}_d^{(S)}(d+L)\,|t_{FS}|^2\right.\right. \\ &\qquad \left.\left. \times\ e^{-\alpha_0^{(F)}\cdot d}\right]\right\}^l, \\ &J_l = \prod_{p=1}^{l}\left[\frac{k\gamma^{(S)}}{\beta^{(S)}} + \frac{i}{2}\,(2p-1)\right], \\ &\psi(z,t) = \tilde{I}_0(t)\cdot\frac{w_0^2}{w^2(z)}, \qquad \tilde{I}_0(t) = \frac{n_0 c\varepsilon_0}{2}\,E_0^2(t), \\ &\mathcal{L}^{(F)}(d) = \frac{1-e^{-\alpha_0^{(F)}\cdot d}}{\alpha_0^{(F)}}, \quad \mathcal{L}_d^{(S)}(d+L) = \frac{1-e^{-\alpha_0^{(S)}\cdot L}}{\alpha_0^{(S)}}, \end{aligned} \tag{6}$$

where t_{AF} and t_{FS} are the air-film and film–substrate transmission coefficients, and $\mathcal{L}^{(F)}$ and $\mathcal{L}_d^{(S)}$ are the effective length in the film and in the substrate, respectively.

The integral of $\mathcal{E}_{\mathrm{AP}}(z,r,t,z_D)$ over r up to the aperture radius (r_a) provides the transmitted power through the aperture:

$$\mathcal{P}_T(z,t,z_D) = n_0\,c\,\varepsilon_0\,\pi\int_0^{r_a}\left|\mathcal{E}_{\mathrm{AP}}(z,r,t,z_D)\right|^2 r\,\mathrm{d}r. \tag{7}$$

Finally, we can calculate the normalized Z-scan transmittance $T(z)$, by including the pulse temporal variation, as:

$$T(z) = \frac{\int_{-\infty}^{+\infty}\mathcal{P}_T(z,t,z_D)\,\mathrm{d}t}{S_a\cdot\int_{-\infty}^{+\infty}\mathcal{P}_i(t)\,\mathrm{d}t}, \tag{8}$$

where $\mathcal{P}_i(t) = \pi w_0^2\tilde{I}_0(t)/2$ is the instantaneous input power within the sample, $S_a = 1 - \exp(-2r_a^2/w_a^2)$ is the aperture linear transmittance, $I_0(t)$ is the on-axis irradiance at focus and w_a denotes the beam radius at the aperture in the linear regime. Given the definition in Eq. (7), which involves a finite r_a value, the expression in Eq. (8) represents itself the model for the CA trace. On the other hand, the model for the OA trace can be readily obtained by setting $r_a \to \infty$ and $S_a = 1$ in Eqs. (7) and (8), since the area of the detector is much larger than the laser spot. Experimentally, S_a represents the fraction of beam transmitted through the aperture and it is estimated as the ratio between the transmitted power measured with and without the aperture (in absence of the sample). As already underlined in [5], the size of the aperture r_a (thus, S_a) represents a crucial parameter for the observation of

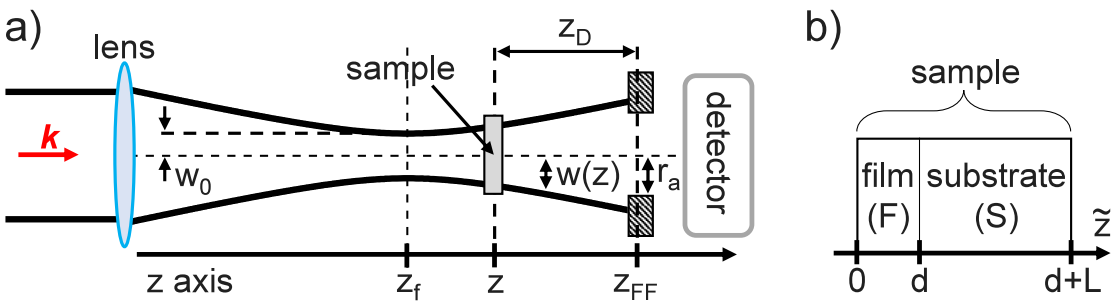

Fig. 1. (a) Sketch of single arm Z-scan experimental setup. (b) Detailed view of the sample structure. **k**: wavevector; w_0: beam waist radius; z_f: focus position; z_{FF}: aperture position; z_D: sample-aperture distance; $w(z)$: beam radius; r_a: aperture radius; d: film thickness; L: substrate thickness.

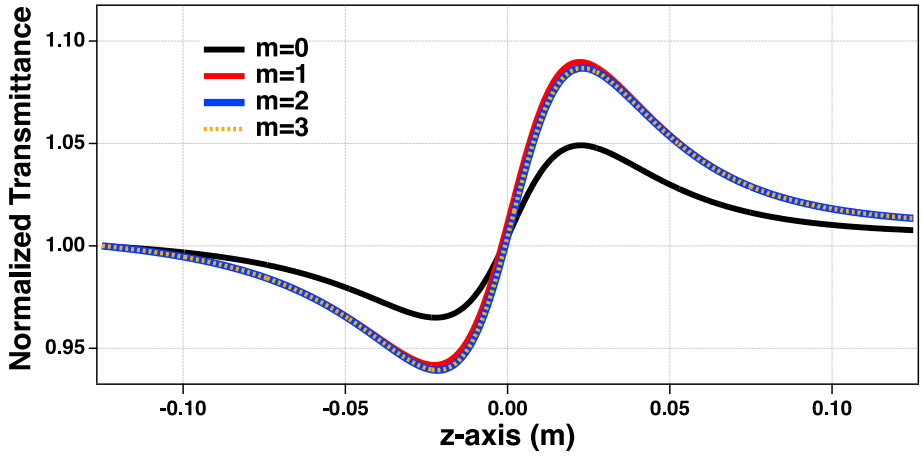

Fig. 2. Z-Scan closed aperture trace considering different orders m of the gaussian beam decomposition obtained from Eq. (8). When $m = 0$ the film contribution is not included. z_F = 15 cm, $\gamma^{(F)} = -1.7 \times 10^{-17}$ m^2/W, $\beta^{(F)} = 9 \times 10^{-13}$ m/W, $\gamma^{(S)} = -1.6 \times 10^{-20}$ m^2/W, $\beta^{(S)} = 5.8 \times 10^{-15}$ m/W, d = 1.2 μm, L = 1.01 mm, $n_0^{(F)} = 1.8814$, $n_0^{(S)} = 1.45$, $I_0 = 3.42 \times 10^{15}$ W/m^2, λ = 1035 nm and $S_a = 0.36253$.

the focusing/defocusing effects in the CA trace. However, since this is beyond the scope of our work, we invite to see the discussion provided in [5]. Fig. 2 displays the normalized transmittance calculated for various values of m to show the convergence of the series expansion in Eq. (5). The case $m = 0$ corresponds to a single layer, as in [5], with thickness $d+L$.

3. Methods

3.1. ITO RF sputtering deposition

The ITO nanolayers used in our experiments are RF magnetron sputtered from an ITO target (In_2O_3/SnO_2 90/10 wt%, purity 99.99%) on transparent fused silica glass. The electro-optical properties of deposited ITO films depend on a number of processing conditions, including substrate temperature, RF sputtering power, deposition pressure, oxygen partial pressure, and post-annealing. The samples were fabricated at room temperature with a RF power of 100 W and Ar sputter pressure of 5 mTorr. The as-is sputtered ITO typically exhibits a plasma frequency above 1800 nm. The samples were post-annealed at 600 °C in vacuum so that a zero-crossing of the real part of the dielectric constant is blue shifted as electron density and/or electron mobility increases.

3.2. Hafnia RF sputtering deposition

RF magnetron sputtering was also employed to fabricate the HfO_2 film. The film was deposited on silicon and vitreous silica glass (v-SiO_2) substrates. The v-SiO_2 substrates have dimensions 75 mm × 25 mm × 1 mm and Si substrates are 25 mm × 25 mm × 1 mm. Before deposition, the substrates were ultrasonically cleaned in deionized water then they were cleaned with ethanol and finally dried in nitrogen. Then, the substrates were also cleaned inside of the RF sputtering chamber for 10 min just before starting the deposition while heating up the temperature to 120 °C at a pressure of 10^{-6} mbar. The magnetron RF sputtering deposition of HfO_2 film was performed using a 15 cm × 5 cm HfO_2 target. The residual pressure before the deposition was 4.5×10^{-7} mbar. During the deposition procedure, the substrates were not heated, and the sample holder temperature was kept at 30 °C. The sputtering was performed in an Ar atmosphere (5.4×10^{-3} mbar) and an RF power of 90 W. To monitor the thickness of the layers during the deposition, quartz microbalance INFICON model SQM-160, faced on the target was employed. The final resolution on the effective thickness obtained by this quartz microbalance is about 1 Å. The deposition time was about 8 h. More details are available in [17].

3.3. ITO ellipsometry measurements

The samples were analyzed using a variable angle spectroscopic (300 nm–1700 nm) ellipsometer (Woollam, VASE) at different incident angles. Using a Lorentz-Drude dispersion model, the complex dielectric constant and film thickness were retrieved. At 1035 nm the complex linear refractive index is $\tilde{n}_0 = 0.996 + 0.176i$.

3.4. Z-Scan experimental setup

A sketch of the experimental setup is displayed in Fig. 3a. A Diode-Pumped Femtosecond Laser (Monaco from Coherent) delivers 300-fs-long pulses with 40 μJ energy (maximum) at 1035 nm wavelength. To prevent heating effects the repetition rate was set to 10 kHz during the

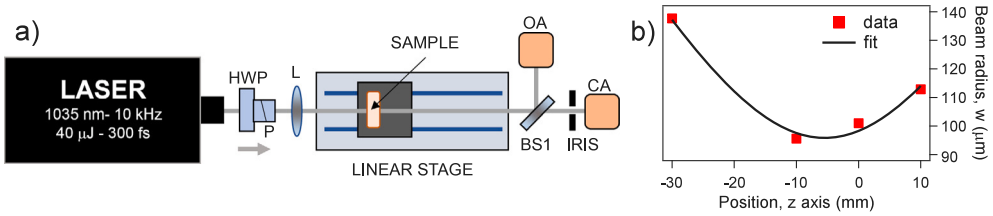

Fig. 3. (a) Schematic of the experimental setup. HWP: Half wave plate; P: Polarizer; L: Lens; BS1: beam splitter; CA: closed aperture photodetector; OA: Open aperture photodetector. (b) Beam radius $w(z)$: experimental data (red markers) and fit (black line).

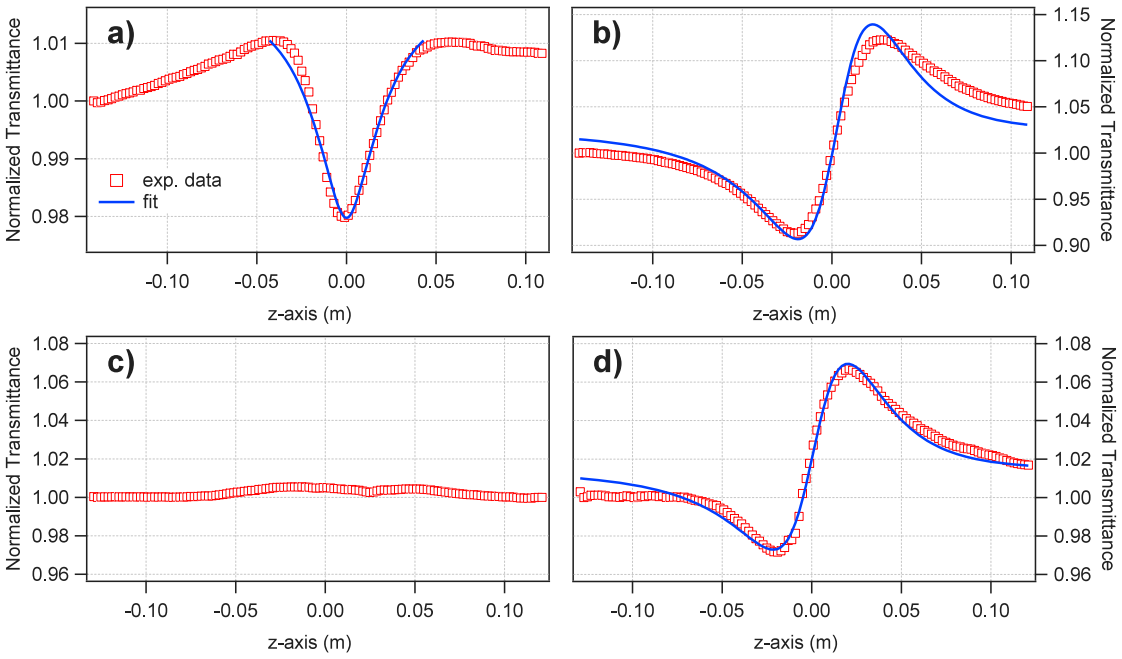

Fig. 4. Open (a) and closed (b) aperture traces measured on a 100-nm-thick ITO film using $I_0 = 5.8$ GW/cm^2 and $S_a = 0.36253$ showing the focusing and two photon absorption effects. Open (c) and closed (d) aperture trace measured on a 100-nm-thick HfO_2 film using $I_0 = 249$ GW/cm^2 and $S_a = 0.36253$. We fit the model in Eq. (8) (blue line) to the experimental data (red markers). (For interpretation of the references to color in this figure legend, the reader is referred to the web version of this article.)

measurements. We use an half wave plate and a polarizer to control the impinging power and the polarization. The light is focused by a 400 mm lens (Thorlabs LA1172-C) and a motorized linear stage (Newport M-ILS250CC) moves the sample along the beam propagation direction. After the interaction with the sample, the transmitted radiation is divided by a beam-splitter into two beams both impinging on a photodetector (Newport Power Meter 2936-R and 9180-UV-OD3R). An iris (Newport M-ID-1.0) is located before one of the two photodetectors in order to obtain the CA trace. The second photodetecor provides the OA trace. The parameter S_a is calculated as the ratio between the power of the beam measured when the iris is closed and when it is open (without the sample). The laser spot size was estimated from a knife edge measurement. In particular, Fig. 3b shows the beam radius at various positions along the z-axis. A theoretical model (black solid line), based on Eq. (2), was fitted to the experimental data (red markers) to retrieve the beam waist radius and it provided $w_0 = (96 \pm 3)$ μm.

4. Results

In this section we compare the results obtained from the traditional model [5] and our model (Eq. (8)) for a thin film of ITO deposited on a silica (SiO_2) substrate. Additionally, we describe the results we obtained with an HfO_2 thin film over a SiO_2 substrate.

4.1. ITO optical measurements

First, we measured the n_2 of the 1-mm-thick SiO_2 substrate (see Appendix C.1). In this case, it is possible to apply the simplified model in [5] to easily obtain the nonlinear refractive index and two photon absorption coefficient. After that, we measure the nonlinear optical properties of the ITO thin film deposited on glass. The linear refractive index of SiO_2 ($n_0 = 1.45$) was taken from [18] and we retrieved the linear refractive index of ITO from ellipsometry measurements (see Section 3.3). InFig. 4a and b, we report the OA and CA traces, respectively. The blue line shows the fit performed with our model. As a comparison, we extracted the γ value of the film employing the theory for bulk materials considering the total contribution to the normalized transmission as the sum of the film and substrate contribution. To do this, we subtracted the contribution to the normalized transmission obtained with the same pumping conditions employed previously to measure the substrate. We attribute the residual transmittance variation to the thin film. Thus, we obtain $\gamma = (8 \pm 1) \times 10^{-18}$ m^2/W, which is two order of magnitude smaller than the previously reported values [7,19]. Now, we apply our model to evaluate the nonlinear coefficients by performing a fit of the OA experimental data with Eq. (8) (see Fig. 4a). The fit is performed with $\beta^{(F)}$ as only free parameter, since the role of $\gamma^{(F)}$ in the OA trace is negligible. Then, the analysis of the CA trace (Fig. 4b) allows to estimate the nonlinear coefficient $\gamma^{(F)}$ by fixing $\beta^{(F)}$.

We obtain an average value of $\beta = (2.10 \pm 0.03) \times 10^{-10}$ m/W and $\gamma = (3.96 \pm 0.08) \times 10^{-16}$ m^2/W at 1035 nm with different intensities for a 100-nm-thick film, which are comparable with [7,19]. Samples with similar thicknesses and increasing impinging intensities provided similar results (see Appendix C.2).

4.2. Hafnia optical measurements

Hafnia is a material with a wide transparency region particularly suitable for nonlinear applications in the visible due to its large bandgap. Despite its potential in nonlinear optical applications, there are few works reporting the n_2 value around $\lambda = 1$ μm but only for bulk material. We set $\beta = 0$ since the material bandgap is much larger than four times the impinging photon energy (5.3 ∼ 5.7 eV [14,20]), see the OA trace in Fig. 4c. Now, we employ our method to extract the nonlinear coefficient of a thin HfO_2 film. We followed the same procedure outlined above. We fitted the CA trace in Fig. 4d and we obtained $\gamma = (1.4 \pm 0.1) \times 10^{-17}$ m^2/W.

5. Conclusions

We exploited a gaussian beam decomposition approach to extend the capabilities of the single arm Z-scan configuration for the characterization of thin film materials. We measured a 100-nm-thick ITO film on silica to experimentally test our model and we obtained $\gamma = (3.96 \pm 0.08) \times 10^{-16}$ m^2/W and $\beta = (2.10 \pm 0.03) \times 10^{-10}$ m/W in accordance with previously reported values. Then, we measured a 100 nm thick HfO_2 film on SiO_2 at 1035 nm and obtained $\gamma = (1.4 \pm 0.1) \times 10^{-17}$ m^2/W. Our results provide a new and reliable tool to extend the Z-scan approach to thin films measurements and other layered nanostructures.

CRediT authorship contribution statement

Andrea Tognazzi: Conceptualization, Methodology, Software, Validation, Investigation, Writing – original draft. **Paolo Franceschini:** Conceptualization, Methodology, Software, Validation, Investigation, Writing – original draft, Visualization. **Thi Ngoc Lam Tran:** Validation, Investigation, Writing – review & editing, Funding acquisition. **Alessandro Chiasera:** Investigation, Writing – review & editing. **Maria Antonietta Vincenti:** Resources, Writing – review & editing, Project administration. **Alfonso Carmelo Cino:** Resources, Writing – review & editing. **Neset Akozbek:** Investigation, Writing – review & editing. **Michael Scalora:** Validation, Resources, Writing – review & editing. **Costantino De Angelis:** Conceptualization, Resources, Writing – review & editing, Supervision, Project administration.

Declaration of competing interest

The authors declare the following financial interests/personal relationships which may be considered as potential competing interests: Thi Ngoc Lam Tran reports financial support was provided by European Research Council.

Data availability

Data will be made available on request

Acknowledgments

A. Tognazzi acknowledges the financial support from the European Union through “FESR o FSE, PON Ricerca e Innovazione 2014–2020 - DM 1062/2021” and the University of Palermo through “Fondo Finalizzato alla Ricerca di Ateneo 2023 (FFR2023)”.

Funding

This work was supported by the European Research Council (ERC) [grant number 816313]

Appendix A. Electric field propagation in the sample

In this section we describe in depth the analytical model regarding the propagation of the electric field within the sample. In the following, the negative (positive) value of γ leads to a focusing (defocusing) effect. A positive value of β describes the two-photon absorption process.

A.1. Film

After the propagation in air, the beam enters in the film and propagates through it. If the sample is located at position z the differential problem shown in Eq. (4) of the main text takes the form (see Appendix A.4 for more details)

$$\begin{cases} \dfrac{\mathrm{d}\Delta\phi}{\mathrm{d}\tilde{z}} = k\,\gamma^{(F)}\,I \\ \dfrac{\mathrm{d}I}{\mathrm{d}\tilde{z}} = -\alpha_0^{(F)}\,I - \beta^{(F)}\,I^2 \\ \Delta\phi(\tilde{z}=0) = 0 \\ I(\tilde{z}=0) = I_0^{(F)} = |t_{AF}|^2\, I(z,r,t) \end{cases} \tag{A.1}$$

where t_{AF} is the transmission coefficient at the air-film interface and $I(z,r,t) = n_0 c\varepsilon_0 |E(z,r,t)|^2/2$ is the intensity of the electric field in Eq. (1) of the gaussian beam just before entering the sample. The differential problem defined in Eq. (A.1) holds for $0 < \tilde{z} < d$, where d is the thickness of the film. We denote $\mathcal{E}_{0F} = t_{AF}\,E(z,r,t)$.

Therefore, for $0 < \tilde{z} < d$, the expressions of the intensity and the phase difference take the form

$$\begin{aligned} I(\tilde{z}) &= \frac{I_0^{(F)}\, e^{-\alpha_0^{(F)}\tilde{z}}}{\beta^{(F)}\, I_0^{(F)}\, \mathcal{L}^{(F)}(\tilde{z}) + 1} \qquad \text{and} \\ \Delta\phi(\tilde{z}) &= \frac{\gamma^{(F)}\,k}{\beta^{(F)}}\,\log\left[1 + \beta^{(F)}\, I_0^{(F)}\, \mathcal{L}^{(F)}(\tilde{z})\right], \end{aligned} \tag{A.2}$$

respectively, where $\mathcal{L}^{(F)}(\tilde{z}) = \left[1 - e^{-\alpha_0^{(F)}\cdot\tilde{z}}\right]/\alpha_0^{(F)}$.

At $\tilde{z} \to d^-$, *i.e.*, on the left side of the film–substrate interface (within the film), the expression for the intensity, phase, and electric field are

$$\begin{aligned} I_{eF} &= I(\tilde{z}=d) = \frac{|t_{AF}|^2\, I(z,r,t)\, e^{-\alpha_0^{(F)} d}}{1 + \beta^{(F)}\,|t_{AF}|^2\, I(z,r,t)\, \mathcal{L}^{(F)}(d)} \\ \Delta\phi_{eF} &= \Delta\phi(\tilde{z}=d) = \frac{\gamma^{(F)}\,k}{\beta^{(F)}}\,\log\left[1 + \beta^{(F)}\,|t_{AF}|^2\, I(z,r,t)\, \mathcal{L}^{(F)}(d)\right] \\ \mathcal{E}_{eF} &= \sqrt{\frac{2I_{eF}}{n_0 c\varepsilon_0}}\cdot e^{i\Delta\phi_{eF}} = t_{AF}\,E(z,r,t)\, e^{-\alpha_0^{(F)} d/2} \\ &\quad \times \left[1 + \beta^{(F)}\,|t_{AF}|^2\, I(z,r,t)\, \mathcal{L}^{(F)}(d)\right]^{i\frac{k\gamma^{(F)}}{\beta^{(F)}} - \frac{1}{2}} \end{aligned}, \tag{A.3}$$

respectively, where $E(z,r,t)$ is the electric field defined in Eq. (1).

A.2. Substrate

The propagation within the substrate ($d < \tilde{z} < d + L$) is analogous to the film case (see Appendix A.1). We denote

$$\begin{aligned} \mathcal{E}_{0S} &= t_{FS}\,\mathcal{E}_{eF} = t_{FS}\,t_{AF}\,E(z,r,t)\, e^{-\alpha_0^{(F)} d/2} \\ &\quad \times \left[1 + \beta^{(F)}\,|t_{AF}|^2\, I(z,r,t)\, \mathcal{L}^{(F)}(d)\right]^{i\frac{k\gamma^{(F)}}{\beta^{(F)}} - \frac{1}{2}}. \end{aligned}$$

The differential problem for the propagation within the substrate region is described as

$$\begin{cases} \dfrac{\mathrm{d}\Delta\phi}{\mathrm{d}\tilde{z}} = k\,\gamma^{(S)}\,I \\ \dfrac{\mathrm{d}I}{\mathrm{d}\tilde{z}} = -\alpha_0^{(S)}\,I - \beta^{(S)}\,I^2 \\ \Delta\phi(\tilde{z}=d) = 0 \\ I(\tilde{z}=d) = I_0^{(S)} = |t_{FS}|^2\,I_{eF} \end{cases} . \tag{A.4}$$

Therefore, for $d < \tilde{z} < d+L$, the intensity and the phase difference take the form (see Appendix A.4 for more details)

$$I(\tilde{z}) = \frac{I_0^{(S)}\,e^{-\alpha_0^{(S)}\cdot(\tilde{z}-d)}}{\beta^{(S)}\,I_0^{(S)}\,\mathcal{L}_d^{(S)}(\tilde{z})+1} \quad \text{and}$$
$$\Delta\phi(\tilde{z}) = \frac{\gamma^{(S)}\,k}{\beta^{(S)}}\,\log\left[1+\beta^{(S)}\,I_0^{(S)}\,\mathcal{L}_d^{(S)}(y)\right], \tag{A.5}$$

respectively, where $\mathcal{L}_d^{(S)}(\tilde{z}) = \left[1-e^{-\alpha_0^{(S)}\cdot(\tilde{z}-d)}\right]/\alpha_0^{(S)}$.

At $\tilde{z} \to (d+L)^-$, *i.e.*, on the left side of the substrate-air interface (within the substrate), the expression for the intensity, phase and electric field are:

$$\begin{aligned} I_{eS} &= I(\tilde{z}=d+L) = \frac{I_0^{(S)}\,e^{-\alpha_0^{(S)}\,L}}{1+\beta^{(S)}\,I_0^{(S)}\,\mathcal{L}_d^{(S)}(d+L)} \\ \Delta\phi_{eS} &= \Delta\phi(\tilde{z}=d+L) = \frac{\gamma^{(S)}\,k}{\beta^{(S)}}\,\log\left[1+\beta^{(S)}\,I_0^{(S)}\,\mathcal{L}_d^{(S)}(d+L)\right] \\ &= \frac{\gamma^{(S)}\,k}{\beta^{(S)}}\,\log\left[1+|t_{AF}|^2\,I(z,r,t)\left[\beta^{(F)}\,\mathcal{L}^{(F)}(d)+\beta^{(S)}\,\mathcal{L}_d^{(S)}(d+L)\right.\right. \\ &\quad \left.\left.\times\,|t_{FS}|^2\,e^{-\alpha_0^{(F)}\cdot d}\right]\right] \\ &\quad -\frac{\gamma^{(S)}\,k}{\beta^{(S)}}\,\log\left[1+\beta^{(F)}\,\mathcal{L}^{(F)}(d)\,|t_{AF}|^2\,I(z,r,t)\right] \\ \mathcal{E}_{eS} &= \sqrt{\frac{2I_{eS}}{n_0 c\epsilon_0}}\cdot e^{i\Delta\phi_{eS}} = \mathcal{E}_{0S}\,e^{-\alpha_0^{(S)}\,L/2} \\ &\quad \times\left[1+\beta^{(S)}\,I_0^{(S)}\,\mathcal{L}_d^{(S)}(d+L)\right]^{i\frac{k\gamma^{(S)}}{\beta^{(S)}}-\frac{1}{2}} \end{aligned} , \tag{A.6}$$

respectively.

A.3. Outside the sample

The electric field at the exit surface of the sample (*i.e.*, $\tilde{z} \to (d+L)^+$) is $\mathcal{E}_{\text{exit}}(z,r,t) = t_{SA}\,\mathcal{E}_{eS}$, which takes the form:

$$\begin{aligned} \mathcal{E}_{\text{exit}}(z,r,t) &= t_{SA}\,t_{FS}\,t_{AF}\,E(z,r,t)\,e^{-\alpha_0^{(F)}\,d/2}\,e^{-\alpha_0^{(S)}\,L/2} \\ &\cdot\left[1+\beta^{(F)}\,|t_{AF}|^2\,I(z,r,t)\,\mathcal{L}^{(F)}(d)\right]^{i\frac{k\gamma^{(F)}}{\beta^{(F)}}-\frac{1}{2}} \\ &\times\left[1+\beta^{(S)}\,I_0^{(S)}\,\mathcal{L}_d^{(S)}(d+L)\right]^{i\frac{k\gamma^{(S)}}{\beta^{(S)}}-\frac{1}{2}}. \end{aligned} \tag{A.7}$$

By recalling Eq. (1) and the definitions of $I_0^{(S)}$, $I_0^{(F)}$, and $I(z,r,t)$, Eq. (A.7) takes the form:

$$\begin{aligned} \mathcal{E}_{\text{exit}}(z,r,t) &= t_{SA}\,t_{FS}\,t_{AF}\,E(z,r,t)\,e^{-\alpha_0^{(F)}\,d/2}\,e^{-\alpha_0^{(S)}\,L/2} \\ &\times\left[1+\beta^{(F)}\,|t_{AF}|^2\,I(z,r,t)\,\mathcal{L}^{(F)}(d)\right]^{i\left[\frac{k\gamma^{(F)}}{\beta^{(F)}}-\frac{k\gamma^{(S)}}{\beta^{(S)}}\right]} \\ &\cdot\left\{1+|t_{AF}|^2\,I(z,r,t)\left[\beta^{(F)}\,\mathcal{L}^{(F)}(d)+\beta^{(S)}\,\mathcal{L}_d^{(S)}(d+L)\right.\right. \\ &\quad \left.\left.\times\,|t_{FS}|^2\,e^{-\alpha_0^{(F)}\cdot d}\right]\right\}^{i\frac{k\gamma^{(S)}}{\beta^{(S)}}-\frac{1}{2}}. \end{aligned} \tag{A.8}$$

The gaussian decomposition for the two phase terms in Eq. (A.8) takes the form:

$$\left[1+\beta^{(F)}\,|t_{AF}|^2\,I(z,r,t)\,\mathcal{L}^{(F)}(d)\right]^{i\left[\frac{k\gamma^{(F)}}{\beta^{(F)}}-\frac{k\gamma^{(S)}}{\beta^{(S)}}\right]} = \sum_{m=0}^{\infty} M_m\cdot e^{-\frac{2mr^2}{w^2(z)}}\cdot P_m \tag{A.9}$$

and

$$\begin{aligned} &\left\{1+|t_{AF}|^2\,I(z,r,t)\left[\beta^{(F)}\,\mathcal{L}^{(F)}(d)+\beta^{(S)}\,\mathcal{L}_d^{(S)}(d+L)\right.\right. \\ &\quad \left.\left.\times\,|t_{FS}|^2\,e^{-\alpha_0^{(F)}\cdot d}\right]\right\}^{i\frac{k\gamma^{(S)}}{\beta^{(S)}}-\frac{1}{2}} = \sum_{l=0}^{\infty} L_l\cdot e^{-\frac{2lr^2}{w^2(z)}}\cdot J_l, \end{aligned} \tag{A.10}$$

where M_m, P_m, L_l, J_l, $I(z,r,t)$, $\psi(z,t)$ and $\tilde{I}_0(t)$ are expressed in Eq. (6).

Thus, Eq. (A.8) may be written as

$$\begin{aligned} \mathcal{E}_{\text{exit}}(z,r,t) &= t_{SA}\,t_{FS}\,t_{AF}\,E(z,r=0,t)\,e^{-\alpha_0^{(F)}\,d/2}\,e^{-\alpha_0^{(S)}\,L/2} \\ &\cdot\sum_{m,l=0}^{\infty} M_m\cdot P_m\cdot L_l\cdot J_l\cdot\exp\left[-\frac{ikr^2}{2R(z)}-\frac{r^2}{w^2(z)}\cdot\left[2(m+l)+1\right]\right]. \end{aligned} \tag{A.11}$$

We note that if the model is adopted to decribe a sample consisting in a film and a substrate of the same material (*i.e.*, a single layer with total thickness $d+L$), the resultant expression of Eqs. (A.8) and (5) matches the corresponding one reported in Ref. [5].

A.4. Solution of the initial value problem

In this section we outline the mathematical procedure adopted to solve the initial value problem defined in Eqs. (A.1) and (A.4). In the two cases, the differential problem can be summarized as

$$\begin{cases} \dfrac{\mathrm{d}\Delta\phi}{\mathrm{d}\tilde{z}} = k\,\gamma\,I & \text{(a)} \\ \dfrac{\mathrm{d}I}{\mathrm{d}\tilde{z}} = -\alpha_0\,I - \beta\,I^2 & \text{(b)} \\ \Delta\phi\left(\tilde{z}=\tilde{z}_0\right) = 0 & \text{(c)} \\ I\left(\tilde{z}=\tilde{z}_0\right) = I_0, & \text{(d)} \end{cases} \tag{A.12}$$

which consists in two coupled first-order differential equations, Eqs. (A.12)(a)–(A.12)(b), and two initial conditions, Eqs. (A.12)(c)–(A.12)(d). First, Eq. (A.12)(b) is solved, since $\Delta\phi$ does not appear in this equation. In particular, Eq. (A.12)(b) is a non-linear first-order differential equation (known as *Bernoulli equation*), which can be transformed into a linear differential equation by introducing the quantity $\Omega(\tilde{z})$, defined as $\Omega(\tilde{z}) = 1/I(\tilde{z})$; therefore, Eq. (A.12)(b) takes the form

$$\frac{\mathrm{d}\Omega}{\mathrm{d}\tilde{z}} = \alpha_0\,\Omega + \beta. \tag{A.13}$$

The first-order differential equation defined in Eq. (A.13) has a general solution of the form

$$\Omega(\tilde{z}) = C_1\,e^{\alpha_0\tilde{z}} - \frac{\beta}{\alpha_0}, \qquad \text{thus} \qquad I(\tilde{z}) = \frac{\alpha_0 e^{-\alpha_0\tilde{z}}}{\alpha_0 C_1 - \beta e^{-\alpha_0\tilde{z}}}, \tag{A.14}$$

with C_1 being a constant to be determined by setting the initial condition provided by Eq. (A.12)(d). This yields to $C_1 = \left(\alpha_0+\beta I_0\right)\cdot e^{-\alpha_0\tilde{z}_0}/\left(\alpha_0 I_0\right)$ and, thus, the solution to the initial value problem defined by Eqs. (A.12)(b) and (A.12)(d) takes the form

$$\tilde{I}(\tilde{z}) = \frac{\alpha_0 I_0 e^{-\alpha_0\cdot(\tilde{z}-\tilde{z}_0)}}{\alpha_0+\beta I_0-\beta I_0 e^{-\alpha_0\cdot(\tilde{z}-\tilde{z}_0)}} = \frac{I_0 e^{-\alpha_0\cdot(\tilde{z}-\tilde{z}_0)}}{1+\beta\,I_0\,\mathcal{L}_{\tilde{z}_0}(\tilde{z})}, \tag{A.15}$$

where

$$\mathcal{L}_{\tilde{z}_0}(\tilde{z}) = \frac{1-e^{-\alpha_0\cdot(\tilde{z}-\tilde{z}_0)}}{\alpha_0}. \tag{A.16}$$

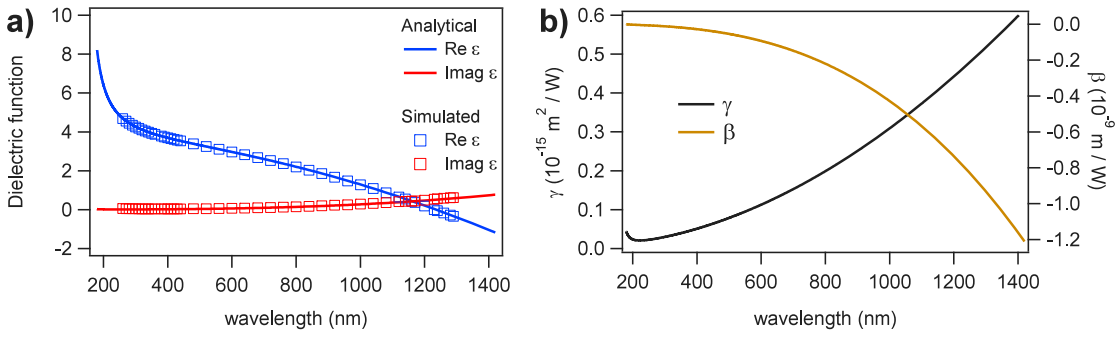

Fig. A.1. (a) Real (blue) and imaginary (red) part of the dielectric function (ε) of ITO simulated with the Maxwell hydrodynamic model (squares) and with the model in [7]. (b) γ (black) and β (yellow) values calculated including non-local contributions in ITO at normal incidence. (For interpretation of the references to color in this figure legend, the reader is referred to the web version of this article.)

Then, the initial value problem defined by Eqs. (A.12)(a) and (A.12)(c) is solved as follows

$$\begin{aligned}\Delta\phi(\tilde{z}) = \Delta\phi(\tilde{z}) - \Delta\phi(\tilde{z}_0) &= \int_{\tilde{z}_0}^{\tilde{z}} \mathrm{d}\zeta\, k\,\gamma\,\bar{I}(\zeta)\\ &= \int_{\tilde{z}_0}^{\tilde{z}} \mathrm{d}\zeta\, \frac{k\gamma\alpha_0 I_0 e^{-\alpha_0\cdot(\zeta-\tilde{z}_0)}}{\alpha_0+\beta I_0-\beta I_0 e^{-\alpha_0\cdot(\zeta-\tilde{z}_0)}}\\ &= \frac{k\gamma}{\beta}\log\left[\alpha_0+\beta I_0-\beta I_0 e^{-\alpha_0\cdot(\zeta-\tilde{z}_0)}\right]\Big|_{\zeta_1=\tilde{z}_0}^{\zeta_2=\tilde{z}}\\ &= \frac{k\gamma}{\beta}\left\{\log\left[\alpha_0+\beta\, I_0\,\alpha_0\,\mathcal{L}_{\tilde{z}_0}(\tilde{z})\right]-\log\left[\alpha_0\right]\right\}\\ &= \frac{k\gamma}{\beta}\log\left[1+\beta\, I_0\,\mathcal{L}_{\tilde{z}_0}(\tilde{z})\right].\end{aligned} \tag{A.17}$$

Appendix B. Retrieval of nonlinear coefficients using Drude-Lorentz oscillator model

As detailed in Ref. [7], the nonlinear oscillator model yields the following analytic expression for the third order complex susceptibility:

$$\chi^{(3)}_{\omega,cgs,ITO} = \frac{3\tilde{\Lambda}}{-\tilde{\omega}^2 - i\tilde{\gamma}_{free}\tilde{\omega}} + \frac{\frac{3\tilde{\beta}}{4\pi^2}\left(\frac{\tilde{\omega}_{pl}^2}{4\pi}\right)^3}{(\tilde{\omega}_{01}^2-\tilde{\omega}^2-i\tilde{\gamma}_{b1}\tilde{\omega})^3(\tilde{\omega}_{01}^2-\tilde{\omega}^2+i\tilde{\gamma}+\tilde{\omega})} \tag{B.1}$$

The first term arises from the free electron (Drude) contribution. The second terms is a Lorentzian resonance located in the 200–400 nm range, as shown in Fig. A.1, where we plot the complex dielectric function for 20 nm-thick layer at normal incidence. Nonlocal effects are not triggered. The Lorentzian resonance is important for THG. The analytic expression above is retrieved [7] from the complex variables depicted in Fig. A.1a.

Since we are interested in n_2 at 1035 nm, we can drop the $\chi^{(3)}(3\omega)$, and invert the expressions for the complex $\chi^{(3)}(\omega)$,

$$\chi^{(3)}_R = \frac{4}{3}n_0^2\epsilon_0 c\gamma \qquad \chi^{(3)}_I = \frac{n_0^2\epsilon_0 c\lambda}{3\pi}\beta \tag{B.2}$$

which assume limited linear absorption.

Table 1
Real ($|\gamma|$) and imaginary ($|\beta|$) part of ITO nonlinear refractive index as extracted from the fit procedure (focusing effect).

$\lvert\gamma\rvert \times 10^{16}$ (m^2/W)				
Intensity (GW/cm^2)	Thickness (nm)			
	20	40	60	100
5.8	15.3 ± 0.7	8.8 ± 0.2	7.5 ± 0.1	3.96 ± 0.08
18	6.7 ± 0.2	3.55 ± 0.06	3.22 ± 0.07	5.68 ± 0.09
53	1.54 ± 0.06	1.91 ± 0.03	2.39 ± 0.06	3.62 ± 0.05
135	–	1.40 ± 0.05	1.84 ± 0.05	2.81 ± 0.06
249	–	1.3 ± 0.1	1.53 ± 0.06	2.36 ± 0.07
Mean value	7 ± 6	3 ± 3	3 ± 2	4 ± 1
$\lvert\beta\rvert \times 10^{10}$ (m/W)				
	Thickness (nm)			
	20	40	60	100
	–	(2.43 ± 0.08)	(2.37 ± 0.08)	(2.10 ± 0.03)

At 1035 nm the curves yield $\gamma \sim 2\times10^{-16}$ m^2/W and $\beta \sim 4\times10^{-10}$ m/W (see Fig. A.1b). The reason β is negative is (probably) due the fact that $\tilde{\Lambda}$ is negative in the expression for $\chi^{(3)}_{\omega,cgs,ITO}$. This differs from ordinary dielectrics like hafnia, because the nonlinearity is triggered by the free electron effective mass, rather than bound electrons, away from resonances.

Appendix C. Z-Scan measurement details

C.1. Silica substrate optical measurements

We performed Z-Scan measurement on the 1-mm-thick SiO_2 substrate, as in Ref. [5]. The obtained OA (red markers) and CA/OA (blue markers) traces are reported in Fig. A.2.

C.2. ITO Z-Scan measurements

In order to validate our model we measured the n_2 value of ITO samples with different thickness. We report the values obtained by the fitting process in Table 1. The dip in the open aperture trace was not appreciable for the 20-nm-thick samples. The expected calculated values are reported in Ref. [7]. We caution the reader that Eq. (3) may not be applicable for local field intensities above 50 GW/cm^2 since it does not include saturation effects.

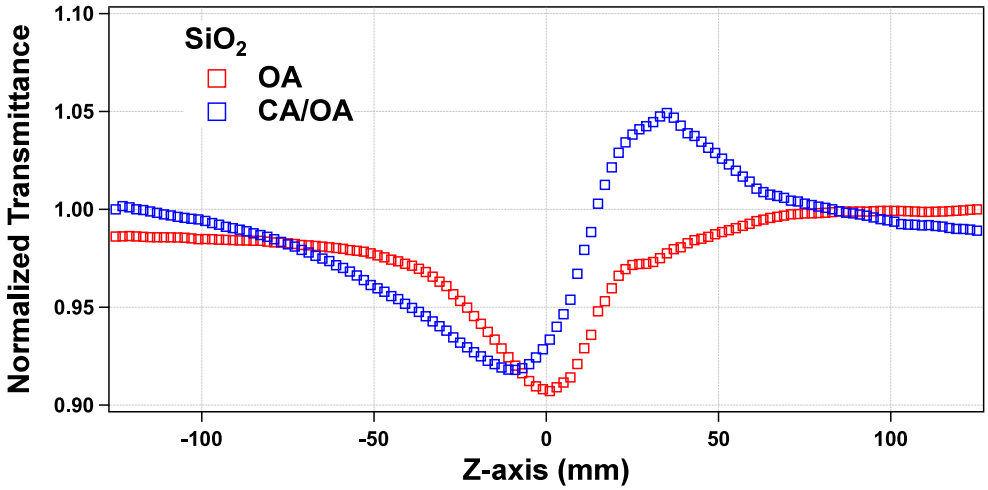

Fig. A.2. Z-Scan traces measured from a 1-mm-thick SiO_2 substrate with I_0 = 249 GW/cm^2 and S_a = 0.36253. (For interpretation of the references to color in this figure legend, the reader is referred to the web version of this article.)

References

[1] P.A. Franken, A.E. Hill, C.W. Peters, G. Weinreich, Generation of optical harmonics, Phys. Rev. Lett. 7 (4) (1961) 118–119.

[2] J. Toulouse, Optical nonlinearities in fibers: review, recent examples, and systems applications, J. Lightwave Technol. 23 (11) (2005) 3625–3641.

[3] D. Malik, G. Kaushik, A. Wason, Performance evaluation of optical amplifiers for high-speed optical networks, J. Opt. Commun. 41 (1) (2018) 15–21.

[4] G. Agrawal, Nonlinear Fiber Optics, Elsevier, 2013, http://dx.doi.org/10.1016/c2011-0-00045-5.

[5] M. Sheik-Bahae, A. Said, T.-H. Wei, D. Hagan, E.V. Stryland, Sensitive measurement of optical nonlinearities using a single beam, IEEE J. Quant. Electron. 26 (4) (1990) 760–769.

[6] A. Mushtaq, B. Pradhan, D. Kushavah, Y. Zhang, D. Naumenko, H. Amenitsch, J. Hofkens, S.K. Pal, Femtosecond induced third-order optical nonlinearity in quasi 2D Ruddlesden–Popper perovskite film deciphered using Z-scan, Mater. Adv. 3 (2022) 8211–8219.

[7] L. Rodríguez-Suné, J. Trull, N. Akozbek, D. de Ceglia, M.A. Vincenti, M. Scalora, C. Cojocaru, Retrieving linear and nonlinear optical dispersions of matter: Combined experiment-numerical ellipsometry in silicon, gold and indium tin oxide, Front. Photon. 2 (2021).

[8] M. Chen, J. Shao, Y. Zhao, G. Hu, M. Zhu, Y. Chai, K. Zhang, H. Ma, High-sensitivity measurements of the nonlinear absorption coefficient of wide bandgap oxide thin films with the Z-scan method, Opt. Mater. Express 12 (2) (2022) 533.

[9] A. Ghanem, M. Zidan, M. EL-Daher, A. Allahham, Thermal lens investigation of the Acid Blue 29 using dual beam z-scan technique, Optik 252 (2022) 168499.

[10] D.V. Petrov, Reflection Z-scan technique for the study of nonlinear refraction and absorption of a single interface and thin film, J. Opt. Soc. Amer. B 13 (7) (1996) 1491.

[11] R.L. Sutherland, Effects of multiple internal sample reflections on nonlinear refractive Z-scan measurements, Appl. Opt. 33 (24) (1994) 5576.

[12] T. Takeuchi, K. Yabana, Extremely large third-order nonlinear optical effects caused by electron transport in quantum plasmonic metasurfaces with subnanometer gaps, Sci. Rep. 10 (1) (2020) 21270.

[13] M.Z. Alam, I.D. Leon, R.W. Boyd, Large optical nonlinearity of indium tin oxide in its epsilon-near-zero region, Science 352 (6287) (2016) 795–797.

[14] C. Zhang, S. Divitt, Q. Fan, W. Zhu, A. Agrawal, Y. Lu, T. Xu, H.J. Lezec, Low-loss metasurface optics down to the deep ultraviolet region, Light: Sci. Appl. 9 (55) (2020).

[15] J. Qin, F. Huang, X. Li, L. Deng, T. Kang, A. Markov, F. Yue, Y. Chen, X. Wen, S. Liu, Q. Xiong, S. Semin, T. Rasing, D. Modotto, R. Morandotti, J. Xu, H. Duan, L. Bi, Enhanced second harmonic generation from ferroelectric HfO_2-based hybrid metasurfaces, ACS Nano 13 (2) (2019) 1213–1222.

[16] F. Tang, X. Ye, Q. Li, H. Li, H. Yu, W. Wu, B. Li, W. Zheng, Quadratic meta-reflectors made of HfO_2 nanopillars with a large field of view at infrared wavelengths, Nanomaterials 10 (6) (2020) 1148.

[17] T.N.L. Tran, A. Szczurek, A. Carlotto, A. Cian, S. Varas, E. Iacob, G. Ischia, O. Sayginer, S. Berneschi, G.N. Conti, R. Balda, J. Fernandez, G.C. Righini, M. Bollani, F. Scotognella, D. Zonta, O. Bursi, P. Gluchowski, A. Lukowiak, M. Ferrari, A. Chiasera, Photon management in SiO_2-SnO_2: Yb^3+ hybrid 1D microcavity, in: Fiber Lasers and Glass Photonics: Materials Through Applications III, SPIE, 2022, http://dx.doi.org/10.1117/12.2620624.

[18] I.H. Malitson, Interspecimen comparison of the refractive index of fused silica, J. Opt. Soc. Amer. 55 (10) (1965) 1205.

[19] M. Ali, A. Shehata, M. Ashour, W.Z. Tawfik, R. Schuch, T. Mohamed, Measuring the nonlinear optical properties of indium tin oxide thin film using femtosecond laser pulses, J. Opt. Soc. Amer. B 37 (11) (2020) A139.

[20] E. Bersch, S. Rangan, R.A. Bartynski, E. Garfunkel, E. Vescovo, Band offsets of ultrathin high-κ oxide films with Si, Phys. Rev. B 78 (8) (2008) 085114.